The influence of interface curvature on solutal Marangoni convection in the Hele-Shaw cell

Mokbel, M.; Schwarzenberger, K.; Aland, S.; Eckert, K.;

Originally published:

August 2017

International Journal of Heat and Mass Transfer 115(2017), 1064-1073

DOI: https://doi.org/10.1016/j.ijheatmasstransfer.2017.08.002

Perma-Link to Publication Repository of HZDR:

https://www.hzdr.de/publications/Publ-24968

The influence of interface curvature on solutal Marangoni convection in the Hele-Shaw cell

Marcel Mokbel[a,d,*], Karin Schwarzenberger[b], Kerstin Eckert[b,c], Sebastian Aland[a,d]

[a] *Institute of Scientific Computing, TU Dresden, 01062 Dresden*
[b] *Institute of Process Engineering, TU Dresden, 01062 Dresden*
[c] *Helmholtz-Zentrum Dresden-Rossendorf, P.O. Box 510119, 01314 Dresden, Germany*
[d] *Faculty of Informatics/Mathematics, HTW Dresden, 01069 Dresden*

Abstract

We study numerically the impact of interfacial curvature onto the Marangoni convection in a two-layer system of immiscible liquids with mass transfer of an alcohol. Assuming a parabolic velocity profile and constant solute concentration across the gap, the simulations solve Navier-Stokes equations coupled to advection-diffusion equations in both phases. Interfacial curvature imposes concentration gradients along the interface as soon as the mass transfer starts. This leads to an immediate interfacial convection which is superimposed later by the onset of the actual Marangoni roll cells. Prominent impact of interfacial curvature onto the Marangoni cells is the occurrence of a *locking* effect, i.e., the Marangoni roll cells adapt to the shape of the interface. Whereas mass transfer is enhanced by interfacial curvature compared to the planar interface in the beginning, *locking* drastically reduces the mass transfer rate. Even for small interface curvature significant differences to the planar case are found, which might explain the accelerated growth of cells in experiments compared to that in numerical simulation recently observed in Koellner et al. [EJP ST 224 (2015), 261-276].

Keywords: Hele-Shaw Cell, Marangoni Convection, Finite Element Method, Interface Curvature

1. Introduction

The Marangoni effect characterizes a flow driven by gradients in surface tension along a fluid-fluid interface. For solutal Marangoni convection, these gradients stem from the concentration distribution of surface-active substances, so-called surfactants. The resulting interfacial flows can exhibit patterning [1] and oscillations [2] and significantly change mass transfer properties. Thereby, many technological applications are affected by Marangoni convection including basic operations in process engineering such as destillation, absorption, and drying[3, 4], liquid-liquid-extraction [5, 6] and new technologies which use the resulting flow structures to pattern functional surfaces [7, 8].

In interfacial mass transfer systems, the solutal Marangoni effect can give rise to instability depending on the material parameters and the direction of mass transfer. According to the linear

*E-mail: marcel-mokbel@gmx.de

stability analysis of Sternling and Scriven [9], the stationary mode of the Marangoni instability occurs when the solute in the donating phase has a lower diffusivity than in the accepting phase provided that viscosity of the latter is lower than that of the donating phase. Characteristic shape of the stationary Marangoni instability is a pattern of roll cells. In contrast to the simple roll cells predicted by the linear theory, the solutal Marangoni instability rapidly develops complex and unsteady flow patterns in experiments, cf. the overview given in [1].

Even though the magnitude of Marangoni convection decreases rapidly with the distance from the interface, it changes the mass transfer rates observed in such systems. This effect, already noted in the early experiments of Sherwood and Wei [10], motivated continuing research on Marangoni flow structures and their relation to mass transfer efficiency [6, 11, 12, 13]. The combination of experimental flow visualization and numerical analysis has recently improved understanding of the mechanisms underlying the evolution of patterns in Marangoni convection [14, 15, 16]. A typical feature is the coarsening of structures, i.e. a steady increase in the size of the Marangoni cells, which compensates for the equilibrated mixing zone inside the cells by entraining fresh fluid [14].

While most experimental studies focus on three-dimensional (3D) setups, the vertical structure of the Marangoni patterns is only accessible from a front view on the two fluids. A simplified access to this vertical structure by optical methods such as shadowgraphy, interferometry and particle image velocimetry is provided by means of the Hele-Shaw (HS) cell. The HS cell is a versatile experimental configuration [17] in which the fluids are enclosed between two parallel plates that are sufficiently close together such that the fluid motion becomes mainly two-dimensional. Also from the viewpoint of theoretical modeling, the HS setup is advantageous since it may be described by a two-dimensional (2D) model based on gap-averaged equations [18], which significantly saves computational cost compared to full 3D simulations. A detailed one-to-one comparison of experimental observations to numerical simulations of solutal Marangoni convection in the HS setup with a planar interface has been presented in [18]. While a qualitative agreement was found between experiments and simulations, the experiments appeared quantitatively accelerated in time. It was hypothesized that the numerical assumption of a planar interface might be the reason for the observed deviation. This hypothesis is further supported by the observation that interface curvature strongly influences Marangoni convection in similar systems [19].

In experiments, interface curvature can result from pinning at small imperfections of the HS plates or flow asymmetries during the filling procedure. Moreover, dynamic interfacial deformations in interaction with a Marangoni-driven flow were observed during reactive mass transfer in the HS cell [20, 21]. These situations call for a study on the influence of interfacial curvature on the Marangoni patterns.

To better understand the impact of interfacial curvature, Finite-Element simulations are performed by using a well-defined experimental system [14, 18, 22, 23]. This system together with the mathematical model is explained in Sec. 2. Numerical simulations are advantageous since interface curvature can be preset at will. To reduce the complexity, we focus on the static case with a defined interface of sinusoidal shape. In Sec. 3, we investigate the influence of differently curved interface profiles (by varying periodicity and amplitude) on the onset of Marangoni instability, the evolution of structures, and the mass transfer rates. Conclusions are given in Sec. 4.

2. Methods

2.1. Considered system

We study Marangoni convection in a two-phase system of two immiscible liquids. Water forms the lower layer and cyclohexanol ($C_6H_{11}OH$) the upper one, see Fig. 1(a). Both phases are in thermodynamic equilibrium due to mutual saturation to reduce effects from phase changes and multi-component diffusion. A weakly surface-active alcohol, 1-butanol (C_4H_9OH), is dissolved in the organic phase (2) at a concentration of 7.5 vol.%, corresponding to a molar concentration of 0.82 mol/l.

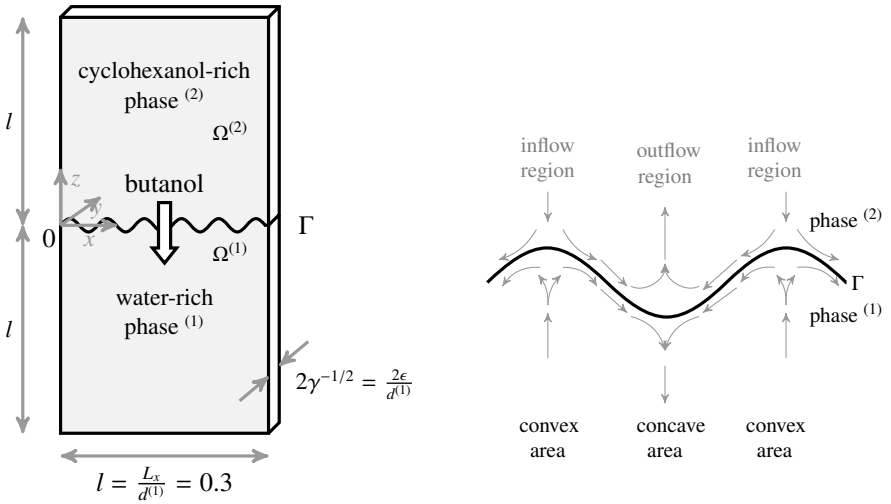

Figure 1: **(a)** Basic setting of the simulations (adapted from [18]), length scales are nondimensionalized by the height of the lower layer, $d^{(1)} = 20\,\text{mm}$, and $L_x = 0.3\,d^{(1)}$ for $i = 1, 2$. **(b)** Typical flow profile of Marangoni convection along a curved interface. Convex and concave areas are defined with respect to phase (1).

The system is placed in a Hele-Shaw (HS) cell in which the gap width between the two solid glass plates amounts to $2\epsilon = 0.5\,\text{mm}$. In contrast to previous studies, assuming initially a plane interface, we consider sinusoidal deformations of the interface as sketched in Fig. 1(a) and defined in Eqs. (13),(14). These deformations are static, i.e. the imposed shape of the interface remains unchanged during the course of the numerical experiment. We restrict the analysis to one principal curvature of the interface. The second principal curvature in the gap of the HS cell is assumed to be infinity which implies a contact angle of ninety degree. We analyse the impact of the sinusoidal deformations onto the pattern of Marangoni cells. The latter appear as a result of the stationary Marangoni instability when the solute (butanol) is transferred out of the organic phase according to the analysis of [9]. Fig. 1(b) sketches the typical velocity profile for the resulting Marangoni flow at such a curved interface. Interface areas are denoted as concave or convex with respect to the lower phase (1). Regions of flow towards and away from the interface are termed as inflow and outflow regions, respectively.

2.2. Mathematical model

We simulate Marangoni convection using a common gap-averaged hydrodynamic model [14, 18, 24, 25]. Therfore, we assume a parabolic flow profile and no solute variation across the gap, an undeformable interface, and an isothermal system. The density $\rho^{(i)}$ of phase (i) and interfacial tension σ depend (affine) linearly on the concentration of butanol $c_b^{(i)}$ with zero excess volume of mixing, i.e.

$$\rho^{(i)} = \rho_{ref}^{(i)} + \rho_{ref}^{(i)} \beta_c^{(i)} c_b^{(i)} \tag{1}$$

$$\sigma = \sigma_{ref} + \sigma_{ref} \alpha_c c_b^{(1)}\,, \tag{2}$$

with the solutal expansion coefficient $\beta_c^{(i)}$, the reference phase densities $\rho_{ref}^{(i)}$, the reference surface tension σ_{ref}, and the butanol specific surface tension coefficient α_c. The other material properties are assumed to be constant in each phase.

The problem is nondimensionalized with the units listed in Tab. 1 (viscous units, see [14, 18]), where c_0 is the initial butanol concentration, $d^{(1)}$ the lower layer height, $\nu^{(1)}$ the kinematic and $\mu^{(1)}$ the dynamic viscosity of the aqueous phase, respectively. The corresponding nondimensional material parameters are listed in Tab. 2. As illustrated in Fig. 1(a), the computational domain is a box $\Omega = [0, l] \times \left[-\gamma^{-1/2}, \gamma^{-1/2}\right] \times [-l, l]$ composed of the two fluid phases $\Omega^{(1)}$, $\Omega^{(2)}$, and the interface Γ. The origin is fixed as the intersection of the left boundary and the interface. In this setting a planar interface would be situated at $z = 0$. In the non-planar case, the interface can be described by a periodic function f as described in Eqs. (10)-(14). We concentrate on the case of a horizontally oriented Hele-Shaw cell. In first approximation, this lets us neglect gravity forces since they act perpendicular to the density gradient.

Table 1: Units of nondimensionalization. The values can be calculated by using the system properties listed in [14, 18].

Unit	Value	Description
c_0	$0.82\ \frac{\text{mol}}{\text{l}}$	molar concentration unit
$\frac{\left(d^{(1)}\right)^2}{\nu^{(1)}}$	333 s	viscous time unit
$\rho_{ref}^{(1)}\left(d^{(1)}\right)^3$	$7.976 \cdot 10^{-3}$ kg	mass unit
$d^{(1)}$	0.02 m	length unit
$\frac{\mu^{(1)}\nu^{(1)}}{\left(d^{(1)}\right)^2}$	$3.59 \cdot 10^{-6}\ \frac{\text{N}}{\text{m}^2}$	unit of pressure
$\gamma = \frac{\left(d^{(1)}\right)^2}{\varepsilon^2}$	6400	gap width coefficient

For modelling, we average the governing three-dimensional flow equations over the gap [18]. Therefore, we apply two assumptions. First, the nondimensional velocity field $\mathbf{u}^{(i)}(x, y, z, t)$ in phase (i) is assumed two-dimensional ($u_y^{(i)} = 0$) with the following parabolic dependence on y:

$$\mathbf{u}^{(i)}(x, y, z) = \frac{3}{2}\left(1 - \frac{y^2}{\varepsilon^2}\right)\left(v_x^{(i)}(x, z)\,\mathbf{e}_x + v_z^{(i)}(x, z)\,\mathbf{e}_z\right). \tag{3}$$

Table 2: System properties of the (cyclohexanol+butanol)/water system. The index $^{(1)}$ marks properites with respect to the water rich phase.

Description	**Symbol**	**Value**
mass density (1)	$\rho_{ref}^{(1)}$	$997\,\mathrm{kg/m^3}$
mass density (2)	$\rho_{ref}^{(2)}$	$955\,\mathrm{kg/m^3}$
kinematic viscosity (1)	$\nu^{(1)}$	$1.2 \cdot 10^{-6}\,\mathrm{m^2/s}$
kinematic viscosity (2)	$\nu^{(2)}$	$20 \cdot 10^{-6}\,\mathrm{m^2/s}$
diffusivity butanol (1)	$D^{(1)}$	$5 \cdot 10^{-10}\,\mathrm{m^2/s}$
diffusivity butanol (2)	$D^{(2)}$	$7 \cdot 10^{-11}\,\mathrm{m^2/s}$
interfacial tension of the binary system	σ_{ref}	$3.4 \cdot 10^{-3}\,\mathrm{N/m}$
change in interfacial tension via $c^{(1)}$	$\sigma_{ref}\alpha_c$	$-8.77 \cdot 10^{-3}$ (N/m)/(mol/l)
solutal expansion coefficient (1)	$\beta_c^{(1)}$	$-0.0172\,\mathrm{l/mol}$
solutal expansion coefficient (2)	$\beta_c^{(2)}$	$-0.0128\,\mathrm{l/mol}$
Schmidt number aqueous phase	$Sc^{(1)} = \frac{\nu^{(1)}}{D^{(1)}}$	2400
Schmidt number organic phase	$Sc^{(2)} = \frac{\nu^{(2)}}{D^{(2)}}$	$2.86 \cdot 10^5$
Marangoni number	$Ma = \frac{c_0\sigma_{ref}\alpha_c d^{(1)}}{\rho^{(1)}\nu^{(1)}D^{(1)}}$	$-2.4 \cdot 10^8$
Partition coefficient	H	31
Density ratio	$\rho = \frac{\rho_{ref}^{(2)}}{\rho_{ref}^{(1)}}$	0.96
Kinematic viscosity ratio	$\nu = \frac{\nu^{(2)}}{\nu^{(1)}}$	16.7
Dynamic viscosity ratio	$\mu = \nu\rho$	16.03
Diffusivity ratio	$D = \frac{D^{(2)}}{D^{(1)}}$	0.14
Ratio of expansion coefficients	$\beta = \frac{\beta_c^{(2)}}{\beta_c^{(1)}}$	0.75

Now let

$$\mathbf{v}^{(i)} = \begin{pmatrix} v_x^{(i)} \\ v_z^{(i)} \end{pmatrix} \tag{4}$$

the two-dimensional gap-averaged velocity. We insert the Hele-Shaw approximation (3) into the three-dimensional Navier-Stokes equations (in viscous units) and average with respect to the y-direction perpendicular to the solid plates. The second assumption is that the nondimensional solute concentration $c^{(i)}$ is constant in y-direction, i.e. $c^{(i)} = c^{(i)}(x, z, t)$.

Hence, we can simplify the three-dimensional Navier-Stokes equations and advection-diffusion

equations for the solute to the two-dimensional Hele-Shaw model in viscous units:

$$\frac{\partial \mathbf{v}^{(1)}}{\partial t} + \frac{6}{5}\mathbf{v}^{(1)}\nabla\mathbf{v}^{(1)} + \nabla p^{(1)} - \nabla\cdot\left(\nabla\mathbf{v}^{(1)} + (\nabla\mathbf{v}^{(1)})^{\mathrm{T}}\right) + 3\gamma\mathbf{v}^{(1)} = \mathbf{0} \tag{5}$$

$$\rho\left(\frac{\partial \mathbf{v}^{(i)}}{\partial t} + \frac{6}{5}\mathbf{v}^{(2)}\nabla\mathbf{v}^{(2)}\right) + \nabla p^{(2)} - \nabla\cdot\left(\mu\left(\nabla\mathbf{v}^{(2)} + (\nabla\mathbf{v}^{(2)})^{\mathrm{T}}\right)\right) + 3\gamma\mu\mathbf{v}^{(2)} = \mathbf{0} \tag{6}$$

$$\nabla\cdot\mathbf{v}^{(1)} = 0\,,\ \nabla\cdot\mathbf{v}^{(2)} = 0 \tag{7}$$

$$\frac{\partial c^{(1)}}{\partial t} + \mathbf{v}^{(1)}\cdot\nabla c^{(1)} - \frac{1}{S\,c^{(1)}}\Delta c^{(1)} = 0 \tag{8}$$

$$\frac{\partial c^{(2)}}{\partial t} + \mathbf{v}^{(2)}\cdot\nabla c^{(2)} - \frac{D}{S\,c^{(1)}}\Delta c^{(2)} = 0, \tag{9}$$

where $\rho = \rho^{(2)}/\rho^{(1)}$, $\mu = \mu^{(2)}/\mu^{(1)}$, $D = D^{(2)}/D^{(1)}$ are the density, viscosity, and diffusivity ratios, respectively. $S\,c^{(1)} = \nu^{(1)}/D^{(1)}$ is the Schmidt number in the aqueous phase (see Tab. 2).

Bottom and top boundaries are considered as impermeable solid walls. We consider an idealized situation in the gap of the HS cell by assuming that the contact angle of the liquid-liquid interface with the glass walls of the HS cell amounts to 90°. This allows us to focus onto the impact of only one principal curvature of the interface. To do so, we prescribe the shape of the liquid-liquid interface by a continously differentiable function

$$f : [0, l] \to (-l, l) \tag{10}$$

and define the interface position by

$$\Gamma = \{(x, f(x))\,|x \in [0, l]\}\ . \tag{11}$$

Hence, $f = 0$ corresponds to a planar interface. To apply the periodic boundary conditions we require

$$f(0) = f(l) = 0, \qquad f'(0) = f'(l) = 0. \tag{12}$$

The interface normal (pointing to $\Omega^{(2)}$) can be written as

$$\mathbf{n} = \frac{1}{\sqrt{f'(x)^2 + 1}}\begin{pmatrix} f'(x) \\ 1 \end{pmatrix}. \tag{13}$$

To vary interface curvature specifically, we simply employ a sinusoidal interface shape. This, for instance, resembles a state of the experiment in [20]. Hence, we have periodic functions f with the following definition:

$$f(x) := K\left(1 - \cos\left(\frac{2\pi B}{l}x\right)\right), \tag{14}$$

where K denotes the amplitude of the interface curve and B denotes the number of periods within the numerical domain. To ensure differentiability over the periodic boundary, f intersects the left and right boundary perpendicularly at $z = 0$.

The interface normal in phase (1) is denoted by $\mathbf{n} = \mathbf{n}^{(1)} = -\mathbf{n}^{(2)}$. We apply a no slip condition for velocity and no solute transport over the top and bottom boundary of the domain Ω:

$$\mathbf{v}^{(1)} = \mathbf{0}\,, \quad \mathbf{v}^{(2)} = \mathbf{0} \qquad \text{for } z \in \{-l, l\} \tag{15}$$

$$\mathbf{n}\cdot\nabla c^{(1)} = 0\,, \quad \mathbf{n}\cdot\nabla c^{(2)} = 0\,. \qquad \text{for } z \in \{-l, l\} \tag{16}$$

In the experiments with the simple mass transfer system described in Sec. 2.1, the interface remains static after the experimental filling procedure [14]. Mathematically, this situation is expressed by vanishing normal velocity of the interface:

$$\mathbf{n} \cdot \mathbf{v}^{(i)} = 0, \tag{17}$$

for $i = 1, 2$. The additional no slip condition is

$$\mathbf{P} \cdot \mathbf{v}^{(1)} = \mathbf{P} \cdot \mathbf{v}^{(2)} \qquad \text{on } \Gamma, \tag{18}$$

where $\mathbf{P} = \mathbf{I} - \mathbf{n} \otimes \mathbf{n}$ is the interface projection operator. Solute mass flux at the interface is assumed to be continuous:

$$\mathbf{n} \cdot \nabla c^{(1)} = D\, \mathbf{n} \cdot \nabla c^{(2)} \qquad \text{on } \Gamma, \tag{19}$$

and concentration equations are coupled by Henry's law:

$$c^{(2)} = H\, c^{(1)} \qquad \text{on } \Gamma. \tag{20}$$

In the face of the static interface condition Eq. (17), the normal component of the stress balance condition becomes redundant, such that only the tangential part remains:

$$\frac{Ma}{S\, c^{(1)}} \mathbf{P} \cdot \nabla c^{(1)} = \mathbf{P} \cdot \left(\nabla \mathbf{v}^{(1)} + (\nabla \mathbf{v}^{(1)})^{\mathrm{T}} - \mu \left(\nabla \mathbf{v}^{(2)} + (\nabla \mathbf{v}^{(2)})^{\mathrm{T}} \right) \right) \cdot \mathbf{n} \qquad \text{on } \Gamma, \tag{21}$$

where Ma is the Marangoni number. In case of a planar interface we recover the simplified equations presented in [18].

Furthermore, we apply periodic boundary conditions at the lateral domain boundaries. Initial conditions are set as follows. Velocities and pressures in both phases are set to zero, initially. There is no butanol concentration in the water rich phase (1), so butanol is only present in layer (2), i.e.

$$c^{(1)}(x, z, 0) = 0 \quad \text{and} \quad c^{(2)}(x, z, 0) = 1. \tag{22}$$

In the planar case, a slight perturbation is necessary to trigger Marangoni convection in our simulations. We add uniformly distributed noise between $\left[0,\ 10^{-3}\right]$ in every grid point of the concentration field. In an initial parameter study for curved interface simulations, we find the overall simulation results independent of the amplitude of the added noise.

There are some problems inherent in our assumptions, which will be discussed briefly in the following. The assumption of a parabolic flow profile may be violated due to geometrical effects or gradients in density or viscosity. A comprehensive discussion on this issue can be found in [18] along with the conclusion that the model we use is recommended. Another problem that might influence the simulation results is Taylor dispersion, i.e. solute transport in the middle of the gap is faster than in the vicinity of the plates. However, in a numerical test of the same chemical system, Koellner et al. [18] find only marginal deviations of the dispersion model compared to our standard diffusion model. Therefore, we neglect Taylor dispersion here.

2.3. Numerical method

The simulations are performed with the finite element method, using the finite element software AMDiS (**A**daptive **M**ulti**Di**mensional **S**imulations), see [26]. The basis is a multi-mesh method with seperate meshes for $\Omega^{(1)}$ and $\Omega^{(2)}$. Our system consists of four different subsystems which are solved sequentially, with suitable boundary conditions applied to every equation (see Tab. 3).

Table 3: Order of solving the problems and applying the relevant boundary conditions on the interface. In every equation, one of the boundary conditions is applied with the right-hand side taken explicitly from previous calculations.

	Problem	**Boundary Condition**
1	Navier-Stokes flow in phase (2)	$\mu\,\mathbf{P}\cdot\left(\nabla\mathbf{v}^{(2)}+(\nabla\mathbf{v}^{(2)})^{\mathrm{T}}\right)\cdot\mathbf{n}=\mathbf{P}\cdot\left(\nabla\mathbf{v}^{(1)}+(\nabla\mathbf{v}^{(1)})^{\mathrm{T}}\right)\cdot\mathbf{n}-\frac{Ma}{Sc^{(1)}}\mathbf{P}\cdot\nabla c^{(1)}$, $\mathbf{n}\cdot\mathbf{v}^{(2)}=0$
2	Navier-Stokes flow in phase (1)	$\mathbf{v}^{(1)}=\mathbf{v}^{(2)}$
3	Concentration equation in phase (1)	$\frac{1}{Sc^{(1)}}\mathbf{n}\cdot\nabla c^{(1)}=\frac{D}{Sc^{(1)}}\mathbf{n}\cdot\nabla c^{(2)}$
4	Concentration equation in phase (2)	$c^{(2)}=Hc^{(1)}$

For the finite element method, Lagrange elements are used with a polynomial degree of 2 for the basis functions, except for pressure, where linear elements are used. A (semi-)implicit Euler time discretization is used. Linear terms are treated implicitly. Nonlinear terms are treated semi-implicitly. The equations are coupled by boundary conditions as displayed in Tab. 3. Thereby, the right hand side of boundary conditions is taken explicitly, i.e., from previous calculations. Time step requirements turned out to be quite strict. In [14], time step adaptivity by the CFL condition is used to calculate every time step. This strategy did not work well for the case of curved interfaces considered here. The time steps calculated with the CFL condition were too large to resolve the concentration dynamics properly. In conclusion, equidistant time steps τ are used with

$$\tau=\begin{cases}10^{-6} & \text{for the first ten steps}\\ 10^{-5} & \text{otherwise}\,.\end{cases} \tag{23}$$

The domain width $l=0.3$ is fixed for every simulation (see Fig. 1(a)). Near the interface, a high grid resolution is required to capture the fine structures arising during Marangoni convection. Hence, adaptive meshes are indispensable. We use a mesh size of $l\cdot 2^{-9}$ length units at a distance of $\leq 10^{-3}$ from the interface; $l\cdot 2^{-7}$ length units in phase (2) in a distance between 10^{-3} and $4\cdot 10^{-2}$ from the interface and for the remaining part of the domain a meshsize of $l\cdot 2^{-5}$ length units in phase (2) and $l\cdot 2^{-4}$ length units in phase (1). In preliminary numerical tests, we verified that the prescribed mesh sizes are well suited to resolve all features of the Marangoni structures.

The simulations are performed with different sinusoidal interfacial deformations in which both the periodicity and the amplitude are varied. The corresponding values for K and B are summarized in Tab. 4. The resulting length L_Γ of the interface, as contained in the 4th column of

Table 4: Overview of performed simulations with different interface curvature (determined by the shifted cosine function f). K denotes the amplitude and B the number of periods in the domain (in nondimensional units). L_Γ is the nondimensional length of the interface.

Name	K	B	L_Γ
Sim_0	0	0	0.3
Sim_1	0.0025	1	0.300062
Sim_2	0.0025	2	0.300247
Sim_4	0.0025	4	0.300985
Sim_{4b}	0.0050	4	0.303910
Sim_6	0.0025	6	0.302208
Sim_{12}	0.00025	12	0.300089

the table are calculated with the arc length formula for f

$$L_\Gamma = \int_0^l \sqrt{1 + f'(x)^2}\,\mathrm{d}x\,. \tag{24}$$

3. Results and discussion

3.1. Variation of interfacial curvature: the qualitative picture

The impact of interfacial curvature, in terms of the number of interface periods, onto the Marangoni convection is examined in Fig. 2. It shows the butanol concentration for Sim_0 and Sim_B for $B = 2, 4, 6$ at $t = 0.5$ and $t = 1.0$. Looking first onto the reference case of the plane interface, Fig. 2(a), (b), we observe a reduction of the number of the cells from initially nine cells at $t = 0.5$ toward six cells at $t = 1.0$. This is the result of a coarsening process of the cells, studied in detail in [14]. Coarsening can be considered as an effective mechanism to reach the partition equilibrium of the solute since the cells get access to fresh bulk fluid with higher solute content.

We now compare the simulations of the reference case, Fig. 2(a) ($t = 0.5$), to the simulations with two and four periods (Fig. 2(c), (e)). Here, another type of coarsening is observed, namely assisted by interfacial curvature, during which the originally nine cells (Fig. 2(a)) decrease to four complete cells in Fig. 2(e). Obviously, weak interfacial curvatures ($B = 2$ and $B = 4$) are also able to force coarsening of the cells. However, stronger curved interfaces inhibit this effect after a while. Indeed, the roll cell sizes of the four-periodic case, Fig. 2(f), exceed the roll cell sizes of the six periodic case, Fig. 2(h). We see that interfacial periodicity slaves the further lateral growth in cell size. The Marangoni cells are in a *locked* state, detailed later on, which is achieved when the roll cell sizes reach the size of the concave interface regions.

The flow structure in terms of a zoom into the velocity field in both phases for $B = 6$ before and after locking in shown in Fig. 3. For further illustration, we also refer to the corresponding movie in the supplementary material. Fig. 3 documents that the Marangoni inflow regions,

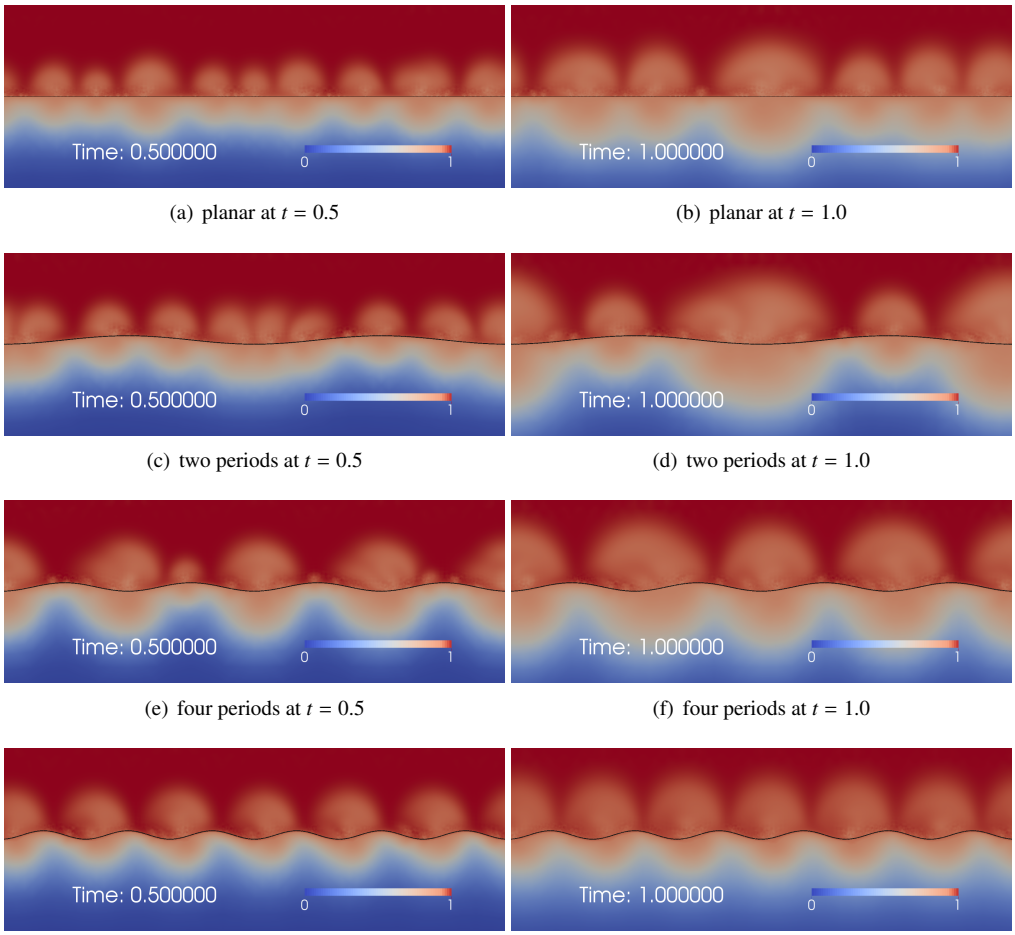

(a) planar at $t = 0.5$ (b) planar at $t = 1.0$

(c) two periods at $t = 0.5$ (d) two periods at $t = 1.0$

(e) four periods at $t = 0.5$ (f) four periods at $t = 1.0$

(g) six periods at $t = 0.5$ (h) six periods at $t = 1.0$

Figure 2: Comparative pictures for the planar case and curved interfaces at $t = 0.5$ and $t = 1.0$. The color scale shows the values of the butanol concentration in layer (2) and $Hc^{(1)}$ in layer (1) with Henry's number $H = 31$. The black line marks the interface.

where the main flow from the bulk impinges on the interface, are located at the convex regions. Accordingly, the outflow occurs in the concave region. Note that the inflow point, marked with C in Fig. 3, can move over time, cf. Fig. 3(a) and (b), which was also observed in experiments with pronounced interfacial curvature [27]. Furthermore, small Marangoni structures occur which are advected by the main flow. This hierarchy of small- and large-scale flow was already observed in the simulations for the planar interface (see Fig. 2(a), (b)) and is a known feature of solutal Marangoni instability [14, 18].

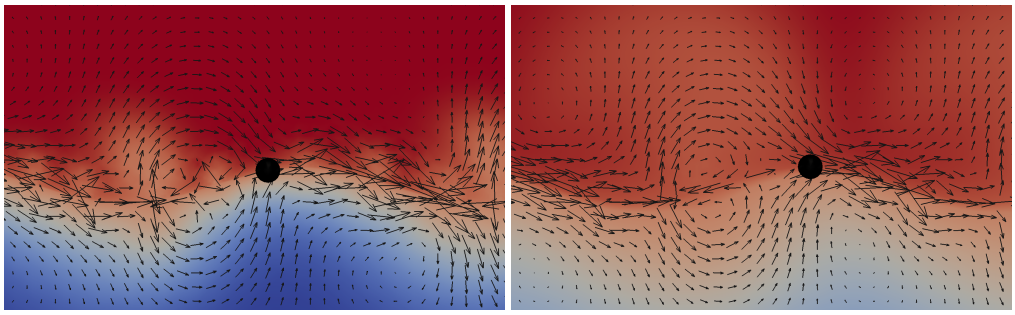

(a) $t = 0.1$ (b) $t = 0.8$

Figure 3: Close up view of velocity fields for six periods at $t = 0.1$ and $t = 0.8$. The color illustrates the values of the butanol concentration in layer (2) and $Hc^{(1)}$ in layer (1) with Henry's number $H = 31$. The color scale is identical to Fig. 2. Arrows illustrate the direction of velocity. The black point marks the large-scale inflow point C mentioned in the text.

3.2. Evolution of interfacial velocity

We next analyze the evolution of the cellular pattern, as documented by their concentration fields in Fig. 2, in terms of the squared interfacial velocity

$$v_m(t) = \frac{1}{L_\Gamma} \int_\Gamma \left\| \mathbf{v}^{(2)}(x, z, t) \right\|_2 \, \mathrm{d}\Gamma \,, \tag{25}$$

for the differently curved interfaces (see Fig. 4(a)). We first look onto the reference case of the plane interface. In the diffusive base state, the system is stable with respect to the Marangoni instability, and $v_m(t) = 0$ until a critical time, t_c. At $t_c \approx 0.01$ the systems becomes unstable and an exponential growth of unstable modes sets in until saturation is achieved at around $t \approx 0.02$. This is in close analogy to [14].

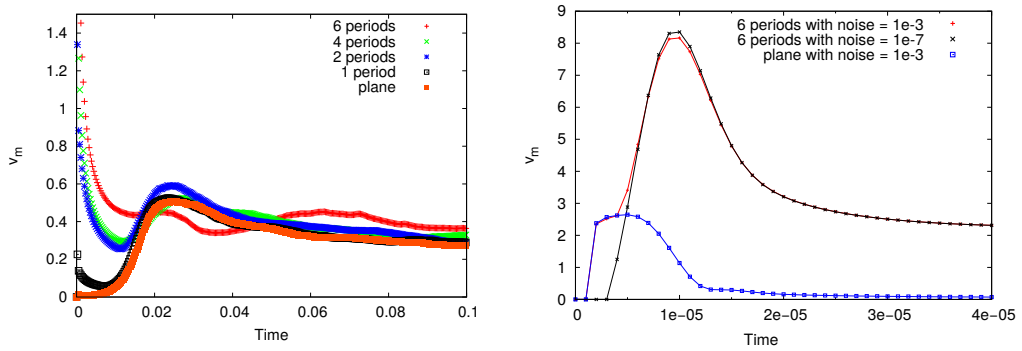

(a) Velocity magnitude over time

(b) Velocity magnitude for the first time steps of the simulation

Figure 4: In (a): Velocity magnitude with v_m defined in Eq. (25) for different interface geometries. All interface curves have an amplitude of $K = 0.0025$. In (b): v_m for the planar case and for six periods. The first time steps of the simulations are shown. The perturbation of concentration in both phases is denoted by `noise`.

On comparing with the curved interfaces, we see similarities for larger times, $t > 0.02$, while significant differences appear at early times. First, the stronger interfacial curvature in

terms of higher values of B, the larger the interfacial velocity at the very beginning. Second, the minimum separating this initial interfacial flow from the onset of solutal Marangoni instability is slightly shifted towards larger times for higher B values. To illustrate the impact of interfacial curvature at the first time steps of the simulations, Fig. 4(b) shows the velocity magnitude with six periods (high interfacial curvature) compared to simulations with a planar interface. While for the planar case the first velocity rise connected with the initial perturbations is quickly damped to values close to zero, it remains at a high level for the strongly curved interface. The influence of initial perturbation (`noise`) of the butanol concentration is negligible. This high level of initial velocity is also seen in Fig. 5(a), (b) by a comparison of the velocity magnitude in both phases for the planar interface and for six periods on the curved interface. Interfacial curvature causes immediate flow into the concave regions, while the system is still at rest for the planar case.

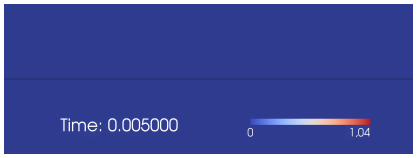

(a) planar at $t = 0.005$

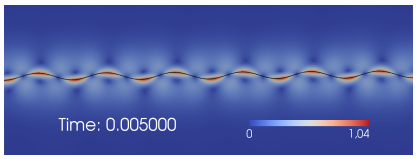

(b) six periods at $t = 0.005$

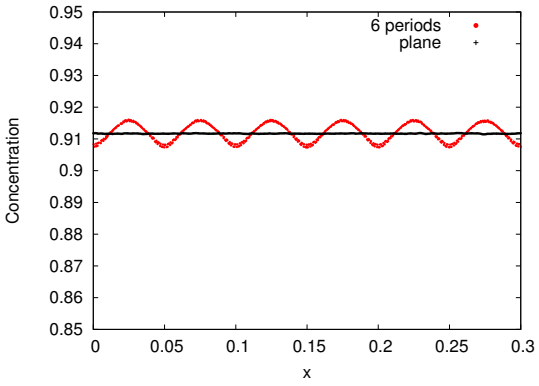

(c) Interface concentration

Figure 5: (a) and (b): Comparison of velocity magnitude for two different simulations at the beginning of the process. (c): Values of $c^{(2)}$ along the interface at $t = 0.005$ when the concentration equations are solved without advection ($\mathbf{v} = 0$).

The origin of the high level of v_m in the systems with curved interfaces becomes readily obvious upon solving Eqs. (8),(9) for pure diffusion, i.e. v=0. We compare this solution in Fig. 5(c) with the analytic one, given in [28] for purely diffusive, one-dimensional mass transfer at a planar interface. Hence, this figure shows the interfacial concentration belonging to the diffusive base states preceding the cellular patterns in Fig. 2(a) and (g). Note that mass transfer proceeds from the top to the bottom layer. On comparing Fig. 5(c) with Fig. 2(g) we see that the interfacial butanol concentration in the upper layer is higher in the convex compared to the concave regions. To understand this, imagine the straight concentration isolines, which run parallel to the *plane* interface in the diffusive base state preceding Fig. 2(a). In order to adapt to the interfacial curvature in Fig. 2(g), these concentration isolines have to bend to follow the sinusoidal curvature. As a result, the concentration gradient in the lower aqueous layer becomes steeper, hence mass flux higher, below the concave regions as compared to the convex ones. Thus, interfacial concentration at the convex places has to be higher, as shown in Fig. 5(c), while interfacial tension is lower. Hence, the diffusive base state imposes gradients in interfacial tension instantaneously, which drives interfacial convection from the very beginning. The underlying Marangoni shear stress, Eq. (21), scales with the interfacial curvature. This explains the higher values of v_m in Fig. 4(a) for stronger curved interfaces. Although v_m of this initial interfacial flow decreases with time, this flow interacts with the Marangoni roll cell instability as described in the following

sections.

3.3. Interface curvature impacts the evolution of structures

Next, we investigate the effect of interface curvature on the evolution of the Marangoni structures. We will concentrate on a comparison of the planar interface simulation to the curved interface simulations with six periods and twelve periods. The correlation between the velocity v_m and the remodelling of Marangoni structures due to merging roll cells is illustrated in Fig. 6. For this purpose, we counted the apparent regions of mixed fluid in the concentration field of phase (2) at different times, appearing as patches of light color above the interface. This gives the number of the large-scale structures as the individual regions of mixed fluid are separated by a large-scale inflow zone while the small-scale cells are not taken into account. We observe a general decrease

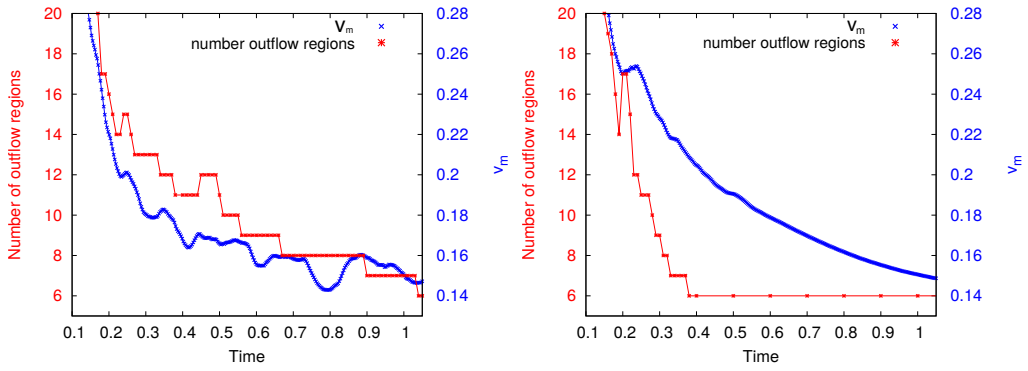

(a) plane (b) six periods

Figure 6: Velocity magnitude v_m defined in Eq. (25) for the planar case (a), six periods (b) in blue compared to the evolution of Marangoni outflow regions in red. The scale of the y-axis on the left side corresponds to the number of outflow regions (red stars), the scale on the right side corresponds to v_m (blue crosses).

in both the number of Marangoni structures and the velocity v_m over time for all simulations. v_m at curved interfaces is higher than for the plane interface since an additional forcing due to the imposed concentration gradients on the interface exists (cf. Fig. 5(c)). In the planar case, we observe decreasing v_m also when no change of the number of Marangoni structures takes place. Vice versa, the velocity magnitude increases, when remodeling takes place, i.e., Marangoni structures arise or merge. For the interface with periodicity $B = 6$, the number of Marangoni structures decreases much faster until locking sets in around $t = 0.4$. *Locking* is caused by the concentration differences imposed along the interface due to differences in the mass transfer between concave and convex regions. The resulting gradients in interfacial tension force an interfacial flow from the very beginning. This large-scale flow interacts with the emerging small roll cells of the Marangoni instability and enhances their coarsening with time by the additional mixing of the near-interface fluid layer. This proceeds until the roll cell size fits in with the shape of the interface and their in- and outflow regions coincide with the large-scale flow. The Marangoni cells remain locked within the interfacial periods since further horizontal growth would imply a motion of the cell boundaries across the convex regions, i.e. across the right margin of Fig. 1(b). As soon as this happens, the Marangoni cell has to work against the oppositely directed Marangoni stress imposed by the neighboring period of interfacial curvature.

This is an unfavorable state which the cell is only able to enter at high Marangoni numbers. In the case of locking, no further restructuring is possible and one observes a smooth decrease of mean velocity magnitude over time in Fig. 6(b). Around $t = 1$, the velocity magnitude v_m for the six periodic case decreases below the values of the planar case.

However, in the experiments for the (cyclohexanol+butanol)/water system in [18, Fig. 2], it can be seen that two neighboring roll cells are able to fuse across a slightly convex interface region. Thus, obviously locking can be prevented under certain circumstances. To demonstrate this numerically, we performed simulations with an interfacial elongation of high periodicity ($B = 12$) but small amplitude ($K = 0.00025$), see Fig. 7. The high value of B leads to a fast locking already at a small roll cell size, but the effect is weak due to low K. Under these conditions, locking, i.e. equality of the number of cells and the number of interface periods, occurs in the time interval $t \in [0.25, 0.5]$. It is accompanied with a strongly decreasing fluid velocity. However, at $t \approx 0.5$, locking is overcome and neighboring roll cells fuse. This remodeling is accompanied by a slight increase in the velocity magnitude. At $t \approx 0.6$, a new temporary equilibrium is reached with eight roll cells.

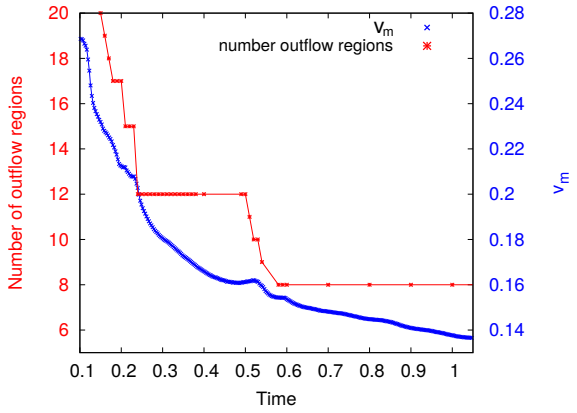

(a) twelve periods

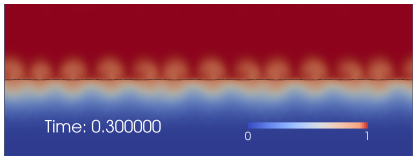

(b) twelve periods at $t = 0.3$

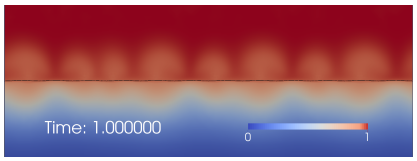

(c) twelve periods at $t = 1.0$

Figure 7: (a): Number of outflow regions and interface velocity for twelve periods. (b) and (c): Corresponding butanol concentration fields illustrating the temporary locking (b) and further remodeling (c).

3.4. Interface curvature increases mass transfer

In this section we address the practical question to which extent interface curvature effects solute mass transport across the interface. Therefore, we examine the mass of butanol in the lower phase

$$m_c(t) = \frac{1}{L_\Gamma} \int_{\Omega^{(1)}} c^{(1)}(x, z, t)\, \mathrm{d}\Omega^{(1)}\,, \tag{26}$$

whereby we scale the integral by L_Γ. This ensures comparable results since more solute is transported over an interface with higher curvature simply due to extended interface length. Fig. 8(a) displays the ratio m_c/m_0, where m_0 is the result of Eq. (26) for the planar interface while m_c is evaluated for simulations with different numbers of periods B and the fixed amplitude $K = 0.0025$. The impact of different amplitudes K at fixed number of periods $B = 4$ is shown in Fig. 8(b).

The curves in Fig. 8(a) and Fig. 8(b) show several characteristic features. With onset of interfacial convection an increase of m_c/m_0 occurs (all values start at unity for $t = 0$). The higher the interfacial curvature (increased by the selection of larger B or K values), the higher the increase. After achieving a maximum, a decrease occurs. This behavior was also found in [1] and discussed there in terms of advection and breakdown of the unstable initial pattern. Afterwards, a slow but steady rise occurs in the phase of coarsening of the Marangoni roll cells which proceeds here also in close analogy to [1] (see e.g. Fig.28). Furthermore, the curves in in Fig. 8(a) and Fig. 8(b) display an offset, i.e. they intersect the y-axis at values larger than unity. In analogy to the previously described increase at the onset of interfacial convection, this offset increases with larger interfacial curvature. This is the fingerprint of the initial interfacial flow driven by the curvature.

Finally, solute transport enhancement generally decreases after locking sets in (marked by black points in Fig. 8), as the growth of Marangoni outflow regions is limited due to the size of the concave regions.

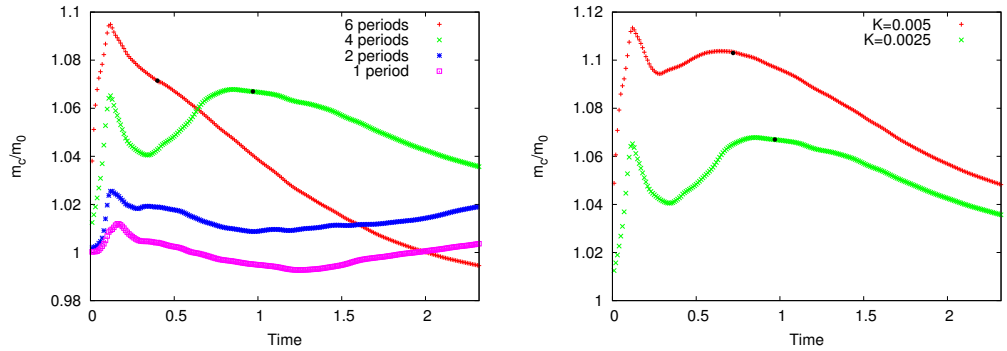

(a) fixed $K = 0.0025$ (b) fixed $B = 4$

Figure 8: Analysis of solute mass transport over the interface. The mass transport ratio m_c/m_0 refers to the result of Eq. (26) for the different simulations, relative to the planar case. In (a), the amplitude is fixed to $K = 0.0025$. In (b), the number of periods is fixed to $B = 4$. Black points mark the time where the number of roll cells begin to match with the number of interface periods (i.e., complete locking).

4. Conclusion

We have investigated the influence of interface curvature on solutal Marangoni convection of a cyclohexanol/water system with mass transfer of butanol in the Hele-Shaw cell. Using finite element simulations with periodically curved interfaces, we demonstrate that interfacial curvature imposes concentration gradients (and therefore surface tension gradients) along the interface as soon as the mass transfer starts. This leads to enhanced mass transfer and hence an accelerated evolution of the Marangoni roll cells after their onset.

As soon as the size of Marangoni structures is comparable to the wavelength of interfacial curvature, a locking effect sets in, i.e., the Marangoni roll cells adapt to the shape of the interface. While this locking effect can be overcome for small interface curvature, it strongly impedes further coarsening and can lead to complete fixation of Marangoni structures for larger curvature.

The observed evolution impacts the efficiency of mass transfer significantly in comparison to a planar interface. There is a clear enhancement of mass transfer in the beginning, but locking effects reduce the transfer rates drastically in later stages.

Even for very small interface curvature, visible differences to the planar case were observed in the evolution of the Marangoni structures. As real interfaces often are not completely planar, this may help to understand deviations between experiments and numerical simulations, for example the accelerated evolution of Marangoni structures that was found in experiments as compared to numerical simulations with a fully planar interface in [18]. Furthermore, these findings suggest that even slight interfacial deformations caused by the Marangoni flow itself can have a significant influence on pattern evolution.

Acknowledgement

We thank Thomas Boeck and Thomas Koellner for stimulating discussion. Financial support by the Deutsche Forschungsgemeinschaft in the framework of Priority Program 1506 is gratefully acknowledged. ZIH of TU Dresden is acknowledged for computing resources.

References

[1] K. Schwarzenberger, T. Köllner, H. Linde, T. Boeck, S. Odenbach, K. Eckert, Pattern formation and mass transfer under stationary solutal Marangoni instability, Advances in Colloid and Interface Science 206 (2014) 344 – 371.

[2] N. Kovalchuk, D. Vollhardt, Marangoni instability and spontaneous non-linear oscillations produced at liquid interfaces by surfactant transfer, Advances in Colloid and Interface Science 120 (13) (2006) 1 – 31.

[3] N. Bassou, Y. Rharbi, Role of Bénard-Marangoni instabilities during solvent evaporation in polymer surface corrugations, Langmuir 25 (2008) 624–632.

[4] F. Doumenc, E. Chénier, B. Trouette, T. Boeck, C. Delcarte, B. Guerrier, M. Rossi, Free convection in drying binary mixtures: Solutal versus thermal instabilities, International Journal of Heat and Mass Transfer 63 (2013) 336–350.

[5] H. Sawistowski, Interfacial convection, Berichte der Bunsengesellschaft für physikalische Chemie 85 (10) (1981) 905–909.

[6] R. F. Engberg, M. Wegener, E. Y. Kenig, The impact of Marangoni convection on fluid dynamics and mass transfer at deformable single rising droplets - A numerical study, Chemical Engineering Science 116 (2014) 208 – 222.

[7] W. Han, Z. Lin, Learning from coffee rings: Ordered structures enabled by controlled evaporative self-assembly, Angewandte Chemie International Edition 51 (7) (2012) 1534–1546.

[8] S.-M. Kang, S. Hwang, S.-H. Jin, C.-H. Choi, J. Kim, B. J. Park, D. Lee, C.-S. Lee, A rapid one-step fabrication of patternable superhydrophobic surfaces driven by Marangoni instability, Langmuir 30 (10) (2014) 2828–2834.

[9] C. Sternling, L. Scriven, Interfacial turbulence: Hydrodynamic instability and the Marangoni effect, AIChE J. 5 (4) (1959) 514–523.

[10] T. Sherwood, J. Wei, Interfacial phenomena in liquid extraction, Industrial & Engineering Chemistry 49 (6) (1957) 1030–1034.

[11] Z.-S. Mao, J. Chen, Numerical simulation of the Marangoni effect on mass transfer to single slowly moving drops in the liquid-liquid system, Chemical Engineering Science 59 (89) (2004) 1815 – 1828.

[12] J. Wang, Z. Wang, P. Lu, C. Yang, Z.-S. Mao, Numerical simulation of the Marangoni effect on transient mass transfer from single moving deformable drops, AIChE Journal 57 (10) (2011) 2670–2683.

[13] M. Wegener, T. Eppinger, K. Bäumler, M. Kraume, A. Paschedag, E. Bänsch, Transient rise velocity and mass transfer of a single drop with interfacial instabilities - Numerical investigations, Chemical Engineering Science 64 (23) (2009) 4835 – 4845.

[14] T. Köllner, K. Schwarzenberger, K. Eckert, T. Boeck, Multiscale structures in solutal Marangoni convection: Three-dimensional simulations and supporting experiments, Physics of Fluids 25 (9) (2013) 092109.

[15] S. Chen, B. Fu, X. Yuan, H. Zhang, W. Chen, K. Yu, Lattice Boltzmann method for simulation of solutal interfacial convection in gas-liquid system, Industrial & Engineering Chemistry Research 51 (33) (2012) 10955–10967.

[16] A. Javadi, M. Karbaschi, D. Bastani, J. Ferri, V. Kovalchuk, N. Kovalchuk, K. Javadi, R. Miller, Marangoni instabilities for convective mobile interfaces during drop exchange: Experimental study and CFD simulation, Colloids and Surfaces A: Physicochemical and Engineering Aspects 441 (2014) 846–854.

[17] Y. Shi, K. Eckert, A novel hele-shaw cell design for the analysis of hydrodynamic instabilities in liquid–liquid systems, Chemical Engineering Science 63 (13) (2008) 3560–3563.
[18] T. Köllner, K. Schwarzenberger, K. Eckert, T. Boeck, Solutal Marangoni convection in a Hele-Shaw geometry: Impact of orientation and gap width, The European Physical Journal Special Topics 224 (2) (2015) 261–276.
[19] K. Schwarzenberger, S. Aland, H. Domnick, S. Odenbach, K. Eckert, Relaxation oscillations of solutal Marangoni convection at curved interfaces, Colloids and Surfaces A 481 (2015) 633–643.
[20] K. Eckert, M. Acker, R. Tadmouri, V. Pimienta, Chemo-Marangoni convection driven by an interfacial reaction: Pattern formation and kinetics, Chaos 22 (3) (2012) –.
[21] M. A. Budroni, L. A. Riolfo, L. Lemaigre, F. Rossi, M. Rustici, A. De Wit, Chemical control of hydrodynamic instabilities in partially miscible two-layer systems, The Journal of Physical Chemistry Letters 5 (5) (2014) 875–881.
[22] E. Schwarz, Hydrodynamische Regime der Marangoni-Instabilität beim Stoffübergang über eine fluide Phasengrenze, 1968.
[23] E. Schwarz, On the occurrence of Marangoni instability, Wärme - und Stoffübertragung 3 (3) (1970) 131–133.
[24] A. Grahn, Two-dimensional numerical simulations of Marangoni-Bénard instabilities during liquid-liquid mass transfer in a vertical gap, Chemical Engineering Science 61 (11) (2006) 3586 – 3592.
[25] D. A. Bratsun, A. De Wit, On Marangoni convective patterns driven by an exothermic chemical reaction in two-layer systems, Physics of Fluids 16 (4) (2004) 1082–1096.
[26] S. Vey, A. Voigt, AMDiS: adaptive multidimensional simulations, Computing and Visualization in Science 10 (1) (2006) 57–67.
[27] Y. Shi, K. Eckert, Orientation-dependent hydrodynamic instabilities from Chemo-Marangoni cells to large scale interfacial deformations, Chinese J. of Chem. Eng. 15 (2007) 748–753.
[28] J. Crank, The mathematics of diffusion, Clarendon Press, Oxford.